RESEARCH PAPER

Smart Digital Image Correlation Patterns via 3D Printing

J. Yang[1] · J. L. Tao[1] · C. Franck[1]

Abstract

Background Digital Image Correlation (DIC) is a popular experimental technique for measuring full-field deformations in materials. Accurate motion and displacement field reconstruction in DIC depend heavily on the intrinsic material texture or speckle patterns painted on the material prior to deformation. Many traditional techniques such as spray painting, ink stamping, or manual texturizing have provided adequate performance but are often challenging to apply on highly compliant, porous or non-planar surfaces.

Objective To address this challenge we present a new, robust and efficient technique to print DIC speckle dot patterns on both planar and non-planar sample surfaces using a custom-modified 3D printer in an automated fashion.

Methods In this new technique, a 3D printer is modified by replacing the conventional extrusion head with a syringe filled with ink. The motion of the 3D printer is controlled via customizable G-code scripts, precisely controlling both the extrusion volume and spatial positioning of the print head in a well-controlled and predictable fashion.

Results The printed speckle dots have radii on the order of $O(10^2)$ µm, and the subsequent DIC reconstructed deformations have an accuracy on the order of $O(10^{-2})$ pixels and $O(10^{-4})$ in measuring displacements and strains, respectively. Furthermore, we demonstrate that this technique has the capability to print suitable patterns for tracking large and heterogeneous deformations in highly compliant and porous materials, as well as materials with significant 3D topographies.

Keywords Digital image correlation (DIC) · Speckle pattern · 3D printing · Non-planar surface

Introduction

Digital image correlation (DIC) is a popular experimental technique for measuring full-field deformations [1–5]. It is well recognized and appreciated that the overall accuracy and precision of any DIC measurement significantly depends on the underlying intrinsic DIC pattern quality [6–9]. Ideally, a quality DIC pattern should meet these basic requirements [6], providing: (i) high contrast: spatially-isotropic varying grayscale intensities and continuous, large intensity gradients; (ii) randomness: non-repetitive patterns to facilitate uniqueness in the full-field displacement results; (iii) isotropy: no directionality in the pattern; (iv) stability: a good speckle pattern is expected to adhere tightly to

the sample surface and deform with the sample (i.e., as a Lagrangian marker). To achieve these characteristics within a DIC speckle pattern, various patterning techniques, summarized in Tables 1 and 2, have been developed, yet several challenges, in particular for printing on highly compliant, and non-planar materials still remain.

For example, the size, density and quality of spray painted speckles often depend on external factors that can be challenging to control precisely including ink viscosity, nozzle size and spray distance. The density and spatial distribution of airbrushed speckles can also be non-ideal due to uneven spraying time [10]. Similar uncertainties exist in other coating or scratching based methods, where pattern quality cannot always be precisely controlled [11–13]. These shortcomings have spawned significant research efforts towards new experimental techniques for designing optimal DIC patterns [14–19]. Some include pattern design via soft lithography or ink jet printing transfer methods [20, 21]. However, lithography methods can be time-consuming to implement in large-scale applications and have limited applicability to compliant or non-planar surfaces. Stamp, inkjet printing, tattoo, or

---

J. Yang and J. L. Tao contributed equally to this work.

✉ C. Franck
cfranck@wisc.edu

1   Department of Mechanical Engineering, University of Wisconsin-Madison, Madison, WI 53706, USA

Table 1 Summary of current popular DIC patterning techniques

No.	Pattern method	Sample material type examples	Selected refs	Printed speckle size	Pros	Cons
1	Natural texture	Materials with inherent micro-structure	[22–24]	10 nm ~1 mm	No pattern fabrication needed	Limited material choices, may produce low quality patterns
2	Airbrush or paint spray	Most materials, e.g., alloys, bio-tissues	[25–28]	1μm ~1 mm	Cheap and easy-to-use, good for both macro and micro applications	Pattern quality is hard to control precisely
3	Tattoo or transfer method	Most materials, e.g., cement composites, alloys	[20, 21]	10μm ~1 mm	Low cost and printed pattern is repeatable and designable	Unstable pattern transfer ratios
4	Stamp or inkjet printing	Most materials, e.g., plastics, alloys	[29]	100μm ~1 mm	Low cost and precise pattern control	Difficult to print on non-planar surfaces and hard to adjust patterns
5	Spin coating	Metals, polymers	[30]	100 nm ~10μm	Low cost and fast	Not easy-to-use for macro-scale applications
6	Particle coating or compressed air method	Alloys	[11]	1 nm ~1μm	Uniform speckle size and pattern quality is consistent	Limited material choice and adherence of particles to the surface can be an issue
7	Nano-film remodeling	Metals, polymers	[31]	1 nm ~100 nm	Pattern morphology can be controlled well	Time consuming and not easy to operate
8	Lithography or focused ion beam	Metals	[32, 33]	100 nm ~10μm	Sample material independent; printed pattern is repeatable and designable	Expensive and time consuming, limited applicability to non-planar sample surfaces
9	Scratching or abrasion or etching method	Metals	[12, 13, 28]	10μm ~1 mm	Simple and inexpensive; no additional painting materials added	Hard to guarantee pattern quality; sample surface is damaged and residual stress can be induced
10	**3D printing method**	**Most materials, e.g., alloys, polymers, bio-tissues**	**Our new method**	**10μm~1 mm**	**Patterns are easily adjustable and precisely controlled for both planar and non-planar surfaces**	**Not currently applicable for sub-micro/nano-scale applications; need to set up a 3D printer and design G-code scripts**

Table 2 Summary of current popular DIC pattern methods in various applications

No.	Pattern method	Natural or artificial (constructive/destructive)	Capability of printing designed patterns	Macro-scale applications	Micro-scale applications	Non-planar sample surfaces	SEM-DIC applications	Extreme high-temperature	Bio-mechanics applications
1	Natural texture	Natural	✗	✓	✓	✗*	✗	✓	✓
2	Airbrush or spray paint	Constructive	✗	✓	✓	✓	✗	✓	✓
3	Tattoo or transfer method	Constructive	✓	✓	✓	✓	✗	✓	✓
4	Stamp or inkjet printing	Constructive	✓	✓	✗	✗	✗	✓	✗
5	Spin coating	Constructive	✗	✗	✓	✓	✓	✗	✓
6	Particle coating or compressed air method	Constructive	✗	✗	✓	✓	✓	✓	✗
7	Nano-film remodeling	Constructive	✗	✗	✓	✓	✓	✓	✗
8	Lithography or focused ion beam	Constructive	✓	✗	✓	✗	✓	✓	✗
9	Scratching or abrasion or etching	Destructive	✗	✓	✓	✓	✗	✓	✗
10	**3D printing method**	**Constructive**	✓	✓	✓	✓	✗	✓	✓

*Most natural patterns are used under SEM or high magnification optical systems to obtain clear images of the inherent microstructure, where planar samples are mostly used

other transfer methods also face significant challenges when applied to non-planar, or highly compliant surfaces.

To address these challenges, we introduce a new patterning technique capable of printing highly repeatable, custom-designed DIC speckle patterns on planar and non-planar, soft and stiff materials. This method, inspired by recent advances in tissue engineering and 3D bio-printing [34], is implemented using open-source tools, making it highly customizable, cost-effective, and automated. Here, a 3D printer is modified by replacing the extrusion tip with a syringe tip filled with ink. The motion of the 3D printer is controlled by executing user-designed G-code files directing both the spatial position and ink extrusion volume of the printer. The G-code data file is compiled with user-assigned speckle dots sizes and positions, which can be easily customized based on the DIC users' application. Our printed speckle dots have typical radii on the order of $O(10)$ μm $\sim O(1)$ mm, with the final DIC tracked deformations providing a resolution on the order of $O(10^{-2})$ pixels and $O(10^{-4})$ in measuring displacements and strains, respectively (cf Assessment of Print Pattern Quality). Because our new technique is built on a 3D printer platform, its prints are highly repeatable and can be executed across small and large specimens in a fully automated fashion. Optimal DIC patterns can be designed a priori accounting for each user's unique application demands. While we demonstrate its capability here to print on non-planar surfaces up to surface angles of 30°, straightforward extensions (e.g., through the inclusion of a sample rotation spindle) can be adapted to facilitate 360° printing if necessary.

The rest of this paper is organized as follows. First, we introduce the experimental setup of our DIC patterning technique in Experimental 3D Printing Setup. The printed pattern can be well controlled by a user-customized G-code script, which directs both the extrusion volume and spatial positioning of each single dot. The relation between the extrusion volume and the printed dot size is discussed in Controlling Printed Speckle Dot Size. In Assessment of Print Pattern Quality, we assess our printed DIC pattern quality by evaluating the DIC measurement errors via synthetic and real experimental examples. Finally, we summarize this paper and provide future directions in Conclusions.
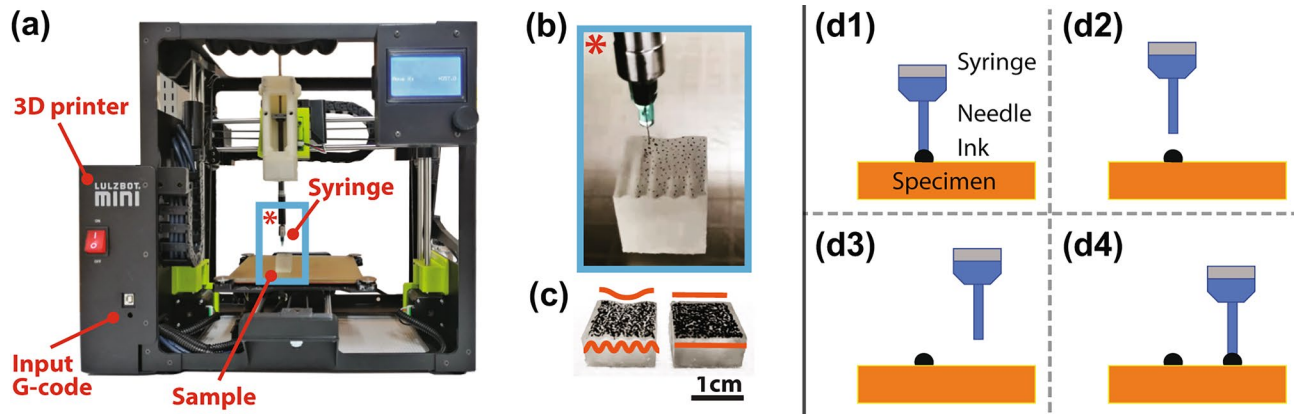
Fig. 1 Experimental setup of a 3D printer to paint DIC speckle dot patterns. **(a)** A 3D printer is modified by replacing the extrusion tip with a syringe filled with ink. The action of the 3D printer is controlled by executing a G-code via a USB connection. Inset (*) is zoomed in **(b)** where a DIC speckle pattern is printed onto a sample. **(c)** Printed DIC patterns on a non-planar sample and a planar sample. **(d)** Pattern printing process: **(d1)** lowering down the extruder close to the sample surface and extruding a certain volume of ink; **(d2)** lifting the syringe needle up; **(d3)** moving the extruder to the center position of the next speckle dot; **(d4)** repeating **(d1)**

Experimental 3D Printing Setup

Modified 3D Printer

The device used to print DIC patterns can be fabricated by modifying most-any extrusion-based 3D printer. In our case, a LulzBot Mini 2 (LulzBot, Fargo, ND) is customized by removing the filament extruder, cooling fans, and filament heaters that are typical of 3D printers. These components are then replaced with a gear-driven ink-filled syringe assembly, where the plunger acts as a direct replacement for the original filament extruder. This direct replacement makes it possible to accurately control the amount of ink that is expelled from a needle by using the same gearing mechanism that once controlled the 3D printing filament extrusion.

3D Printing Control via Customized G-Codes

The significant advantage of our proposed DIC patterning technique is that each dot location and size can be precisely controlled via a customized G-code, a common language used for controlling 3D printers [35]. In general, a G-code file is composed of three parts: *start part*, *main body* and *end part*. In the *start part*, the initial coordinates of the needle's position (x, y, z) and extrusion are set to a reference state after a prime extrusion is set. The *main body* part of the G-code follows the steps outlined in Fig. 1(d1−d4) to control the position of the needle and the extrusion volume of the ink transferred to the sample's surface (see Controlling Printed Speckle Dot Size for more details about controlling speckle dot size). During the actual printing cycle the needle tip is in close proximity to the top surface of the sample but is typically programmed to avoid coming in direct contact with the surface. In the *end part*, the extruder is moved away from the sample surface and its motor turned off.

In practice, the size and spatial density of DIC pattern dots can be further determined by implementing DIC pattern optimization rules [14–19]. Typically, the diameter of each pattern dot is expected to be $2 \sim 5$ px, (px: pixels) [36] and the total area of printed dots covers $40 \sim 70\%$ of the sample surface [37]. The center position of each dot is pseudo-randomly distributed [17, 18], e.g., generated from a Poisson-disc sampling procedure [38], to guarantee the uniqueness of the DIC tracking results [18]. A list of G-code commands used to control the 3D printer motion are summarized in Appendix A.

Controlling Printed Speckle Dot Size

In our proposed DIC pattern technique, each individual speckle dot is printed by extruding a single droplet of prescribed ink volume from the 3D printer needle tip. The size of the printed speckle dot can be accurately predicted from a simple theoretical model and input into the G-code file, where the size and shape of the printed speckle dot depends on the contact angle between the ink liquid and the sample's top surface, extruded volume during each print step, and the slope of the sample's surface. In this section, we describe the theoretical model and compare it to experimental measurements as validation.
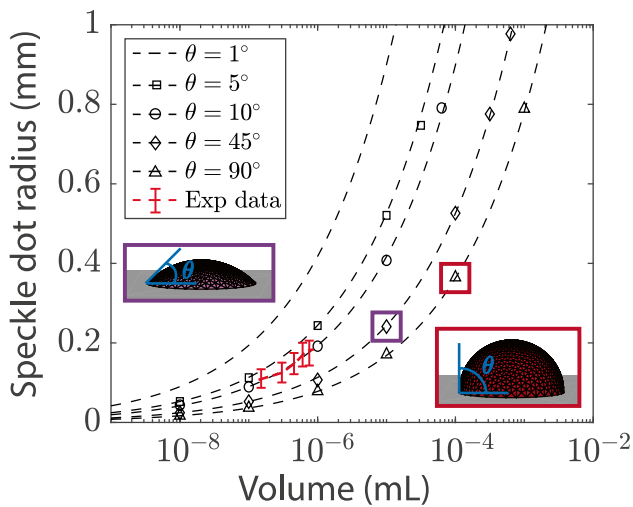
Fig. 2 Scaling relationship between the printed speckle dot radius and 3D printer extrusion volume for various ink-sample surface contact angles. Dashed lines show Eq (1) with discrete markers provided by the numerical solutions of the Young-Laplace equation using the software Surface Evolver [39]. Two insets are illustrations of how ink droplets, with two different contact angle values are printed onto the sample surface

Fig. 3 Designed and printed speckle patterns. (i) Designed DIC patterns where speckle dots are following a Poisson disc sampling with a spatial density of 1200 dots per square inch. Each speckle pattern was printed with increasing extrusion volume: **(a)** 1.5×10^{-7} mL, **(b)** 3.0×10^{-7} mL, **(c)** 4.5×10^{-7} mL and **(d)** 6.0×10^{-7} mL. (ii) Experimentally printed DIC patterns are in good agreement with their designed pattern templates in (i), (see red markers in each sub-figure; scale bar: 2 mm). (iii) Statistics plots of the radii of experimentally printed speckle dots

Theoretical Model

We begin by considering the simplest case: printing a DIC pattern onto a planar sample surface, where each single speckle dot has a perfect circular shape and its radius, r, is the radius of the bottom contact area between the ink droplet and the sample surface, obeying the following relation[1]:

$$r = \left[\frac{3\sin^3\theta}{\pi(2 + \cos\theta)(1 - \cos\theta)^2} V \right]^{1/3}, \quad (1)$$

where θ is the contact angle between the ink liquid and the sample's top surface, and V is the extrusion volume during each print step. Equation (1) is plotted as dashed lines in Fig. 2. We also conducted numerical simulations minimizing the interfacial energy between the ink and surface using the software Surface Evolver [39]. Results are plotted in Fig. 2 using hollow markers and overlaid with Eq (1).

From Fig. 2, we find that the radius, r, of each individual printed speckle dot generally scales with the extrusion volume, V, as $r \propto V^{1/3}$. For the same droplet volume, the smaller contact angle of the liquid ink generates a larger individual speckle dot, because it is of a shallower shape before final evaporation. Two examples of extruded droplets are

visualized in Fig. 2 insets: the left inset shows an extruded 10^{-5} mL ink droplet with a surface contact angle of 45° forming a shallow dome shape, while the right inset features an extruded 10^{-4} mL ink droplet with a surface contact angle of 90° forming a hemispherical shape. The final speckle dot radius is measured after the deposited ink has dried completely.

Experimental Validation of Printed DIC Pattern

To assess the practical validity of Eq (1), we printed various DIC patterns guided by Eq (1) and measured the final printed dot radii as shown in Fig. 3. Here, a glass syringe (Hamilton, Franklin, MA) is first filled with black acrylic ink (Liquitex Artist Materials, Piscataway, NJ) and installed into the 3D printer to extrude ink droplets onto a highly compliant polyurethane-based open-cell elastomeric foam (Poron XRD, Rogers, CT), which will further be analyzed using DIC in Case Study II: Uniaxial Compression Test. The surface contact angle between the foam and the ink was measured to be around 10° by least square fitting Eq (1) against the experimentally measured printed speckle dot radius vs. single dot extrusion volume curve, as shown in Fig. 2. The inner diameter of the syringe needle in our experiments is 150 μm. We tested four different extrusion volumes ranging from 1.5×10^{-7} mL to 6.0×10^{-7} mL with a fixed spatial density of 1200 dots per square inch. Special care was exerted to prevent individual ink droplets from overlapping (Fig. 3; first row). The input designs are shown in Fig. 3(i). The resulting experimentally printed

---

[1] Final speckle dot radii may be smaller than Eq (1) if there are contact angle hysteresis and pinning effects during the ink liquid evaporation process. However, these effects were not observed in our experiments.
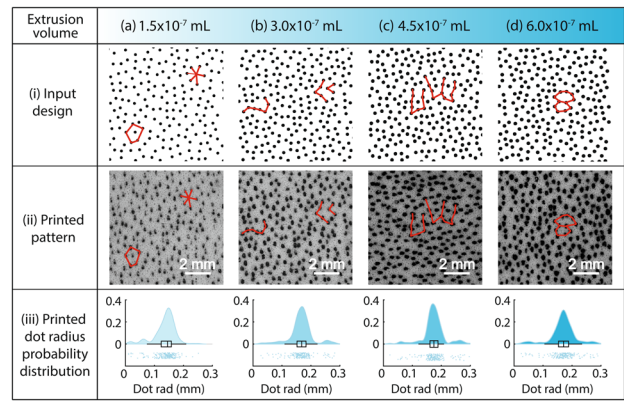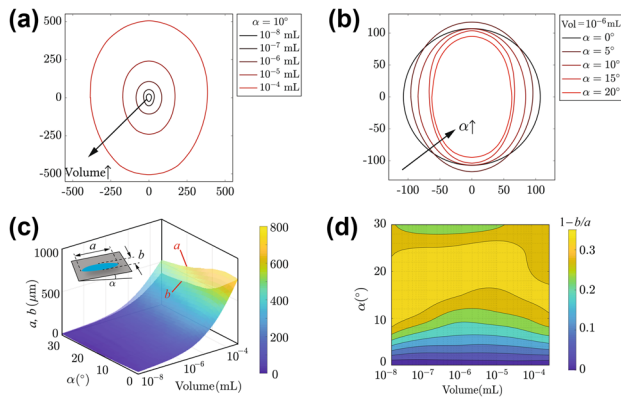
Fig. 4 The effects of sample surface topography (i.e., slope) on the eccentricity of printed DIC speckles. (a) Simulated speckle dots whose volumes change from 10^{-4} mL to 10^{-8} mL on a non-planar sample surface with a slope of 10°. (b) Simulated speckle dots with a fixed volume 10^{-6} mL on an angled surface with slopes changing from 0° to 20°. (c–d) Simulated a, b, and eccentricity, $(1 - b/a)$, with various ink extrusion volumes and surface slopes, where a, b are defined in the inset of (c)

DIC patterns are presented in Fig. 3(ii), which are in good agreement with the original designed patterns. The radii of all the printed speckle dots are further analyzed and summarized in Fig. 3(iii) with a general size distribution ranging from 100~200 μm, corresponding to 5px~10px in the images in Fig. 3(ii). All experimentally measured speckle dot radii are in good agreement with their theoretical predictions given by Eq (1) (see red vertical line style markers in Fig. 2).

Printing DIC Patterns on Non-Planar Surfaces

A big advantage of using a 3D printer over conventional 2D printing techniques is the ability to print on more complex-shaped 3D surfaces. To demonstrate this capability, we used our 3D printing method to deposit a custom DIC pattern on a sinusoidal 3D surface of varying frequency (see Fig. 1(b)). Since the print head needs to be programmed to trace the 3D topography of the sample to deliver the precise print pattern, the user must first supply the 3D surface coordinates to the G-code, which can be obtained via common 3D metrology techniques (e.g., 3D surface scanning [40]).

To quantitatively evaluate the effects of the sample topology on the final printing pattern, we numerically simulated the printed speckle shape evolution as a function of the local sample surface slope angle, α, and the ink extrusion volume, V, using the software Surface Evolver [39, 41] as before. We find that for a given surface slope, all printed speckle dots maintain an almost fixed shape (Fig. 4(a)). For a given extrusion volume, the eccentricity
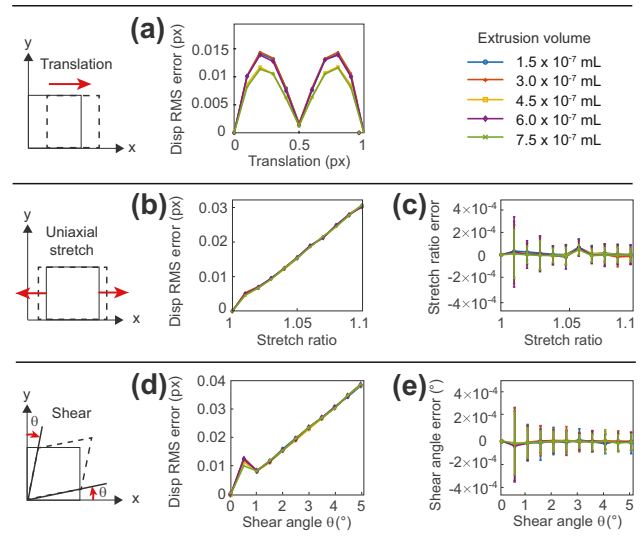

Fig. 5 Quantitative assessment of the printed DIC patterns shown in Fig. 3(ii) via synthetically-applied deformations. (a, b, d) The displacement RMS error for the synthetically applied rigid body translation (a), uniaxial stretch (b), and pure shear (d) deformations. (c, e) Error bar plots of DIC reconstructed uniaxial stretch ratios (c) and shear angles (e)

of the printed speckle dot increases as the sample surface slope increases (see Fig. 4(b)). However, the resulting eccentricity $(1 - b/a$, see inset of Fig. 4(c) for definitions of a, b) remains less than 0.3 as long as the surface slope is within 30°.

Assessment of Print Pattern Quality

In this section, we assess our printed DIC pattern quality via both synthetic and real experimental examples. In the synthetic examples, we apply various types of known deformations to deform the reference image to mimic mechanical loadings, followed by DIC analysis of the virtually applied deformations. Similarly, in the real experimental example, a sample is painted using our proposed pattern technique and then uniaxially compressed to about ∼ 40% nominal compressive strain. The sample compression process is recorded with a digital camera set at a framing rate of 0.5 frames per second (fps). Finally, the recorded image sequence is post-processed using our recently developed augmented Lagrangian DIC (ALDIC) method and the commonly used local subset inverse compositional Gauss-Newton (ICGN) method [5]. Finally, to demonstrate that our technique can produce high quality speckle patterns on 3D, non-planar surfaces, we applied our printing method to a specimen with significant 3D surface undulation and tracked its displacement and strain fields during a simple uniaxial tension test using a 3D stereo-DIC system.

Case Study I: Synthetic Deformation

First, we assess our printed pattern quality by applying three types of known synthetic deformations, i.e., rigid body translation, uniaxial stretch, and pure shear, and then compare the original and DIC-reconstructed displacement fields.

We apply each synthetic deformation to an 8-bit, gray-scale image of final size of 401 px by 401 px depicting a cropped region of interest from the images shown in Fig. 3(i). The imposed rigid-body translations are along the x-direction ranging from $0.1 \sim 1$ px with an increment of 0.1 px. The imposed uniaxial stretches are along the x-direction with stretch ratios ranging from $1.01 \sim 1.1$ with an increment of 0.01. The pure shear deformations are defined with prescribed shear angles ranging from $0.5° \sim 5°$ with an increment of 0.5°. Schematic diagrams of all these three types of deformation are shown in the left column of Fig. 5. To generate the deformed images, we used a bicubic spline interpolation scheme to interpolate the grayscale values at subpixel locations [42]. No additional noise terms are applied to the synthetically deformed images. Next, we apply an ICGN local subset DIC algorithm where the DIC measurement error is proportional to the inverse of the sum of squares of the subset intensity gradients (SSSIG) [18][2].

All the resultant displacement and deformation gradient fields are extracted after the convergence of the local ICGN algorithm with a subset size of 64 px by 64 px, and a subset spacing of 16 px by 16 px. The measured displacements ($\hat{u}_x^i$ and $\hat{u}_y^i$) for each subset of each image pair can be compared directly to the imposed true displacements (u_x^i and u_y^i). The root mean square (RMS) error among all the n subsets within one deformed image is used as a metric to evaluate the error level of the DIC analysis per given input pattern, and is defined as:

$$\text{RMS error} = \sqrt{\sum_{i=1}^{n} \frac{\left(u_x^i - \hat{u}_x^i\right)^2 + \left(u_y^i - \hat{u}_y^i\right)^2}{n}} \qquad (2)$$

The RMS error in the solved displacements are summarized in Fig. 5(a, b, d), and error bar plots of the computed uniaxial stretches and shear angles are summarized in Fig. 5(c, e), respectively. We find that the RMS error in the solved displacements is within 0.015 px for all of the small deformations (rigid body translations, uniaxial stretches with stretch ratio less than 1.05, and pure shears with shear angle less than 3°), which is similar or even better when compared to DIC patterns generated with other popular methods [15, 16, 19, 29, 44]. The displacement error increases for large deformations, however, still remains on the order of $O\left(10^{-2}\right)$ px. In addition, we find that the error in the measured deformation gradients and stretch ratios and shear angles maintains a relatively low level on the order of $O(10^{-4})$, and does not increase significantly as the deformation magnitude increases. For all of our evaluated patterns, the extrusion volume of each speckle dot does not show strong effects on the accuracy of the final reconstructed deformations. In general, our printed patterns provide high accuracy during DIC post-processing, with displacement and strain measurement precisions $\sim O(10^{-2})$ px, and $O(10^{-4})$, respectively.

Case Study II: Uniaxial Compression Test

In order to assess the suitability of our printed DIC patterns during an actual experiment, we performed a large deformation uniaxial compression experiment on an open-cell polyurethane foam sample (Poron XRD, Rogers, CT with a nominal weight density of 240.3 kg/m^3) comparing the DIC displacement data with its cross-head data. The dimensions of the foam specimen were approximately $12.7 \times 12.7 \times 12.7$ mm^3 where the camera-facing sample surface was printed with 600 speckle dots using a syringe tip of inner diameter of 80 µm filled with acrylic ink (Liquitex Artist Materials, Piscataway, NJ) at an extrusion volume of 2.07×10^{-8} mL. All of the painted speckle dots follow the aforementioned Poisson disc sampling rule [38].

The experimental setup consists of the same elements as previously described in Landauer et al. [27]. Briefly, a screw-driven linear actuator (Ultra Motion, Cutchogue, NY) with a ballpoint tip is employed for imparting uniaxial compression via a top steel platten and a load cell (LCFD-50, Omega Engineering, Stamford, CT) is connected to a custom-built LabView (National Instruments, Austin, TX) interface allowing synchronization of the actuator displacement, imaging, and force data collection components (see more details in [27]). The optical system for DIC image collection is composed of a scientific PCO Edge5.5 camera (edge5.5, PCO-Tech Inc., Romulus, MI) and a long-distance microscopy lens (K2/S, Infinity Photo-Optical Company, Boulder, CO) along with two LED light panels (Lykos Daylight, Manfrotto, South Upper Saddle River, NJ).

Proper resolution of displacement and strain fields can be challenging for highly porous and compliant materials, and we recently presented two new DIC methods that perform well under such circumstances, namely q-FIDIC [4, 27], and

---

[2] Other DIC methods, for example, FE-based global DIC, q-FIDIC [3, 4], ALDIC [5, 43], could achieve better accuracy than the ICGN local subset DIC algorithm. However, the error of ICGN local subset DIC method is a useful metric in pattern quality assessment as its error correlates well and proportionally to the information encoded in the images.
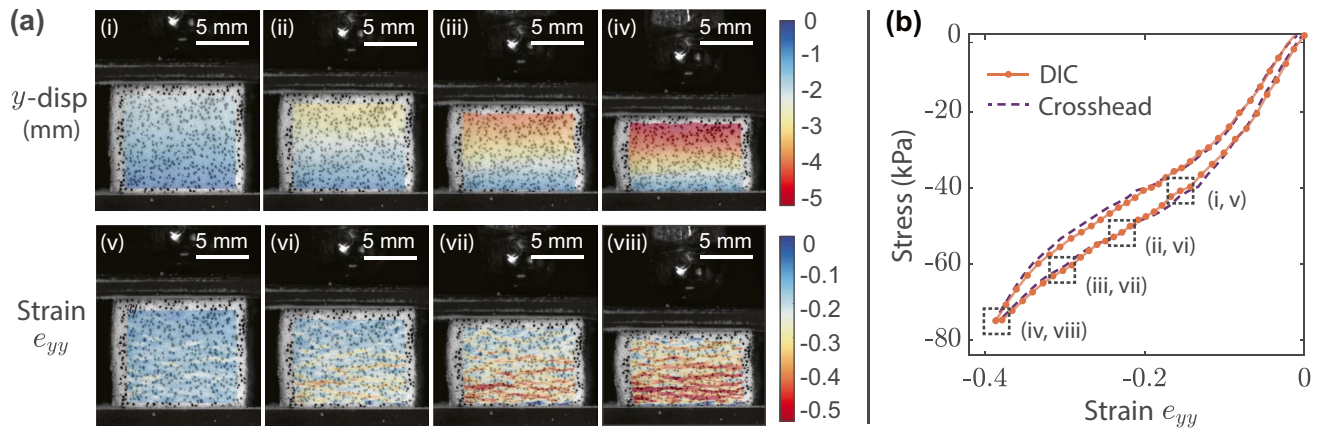
Fig. 6 Uniaxial compression experiment using 3D printed DIC pattern. **(a)** ALDIC full-field y-displacements (i-iv) and e_{yy} strains (v-viii) at four time points during the compression load cycle (dashed squares in **(b)**). Localization bands due to slight surface imperfec-tions are clearly visible and well-resolved using the printed DIC pattern (scale bar: 5 mm). **(b)** Stress-strain curve comparing strain data derived from ALDIC and crosshead data

ALDIC [5, 43]. Here, we apply the ALDIC method to evaluate the suitability of our printed patterns in resolving large and partially heterogeneous deformations. For all ALDIC calculations the subset window and step size are set to 64 px by 64 px and 16 px by 16 px, respectively, and the image sequence is post-processed cumulatively comparing all deformed images to a single, fixed and stress-free reference image (typically the first image prior to loading application).

Figure 6(a)(v-viii) plots spatial variations in the compressive strain ($e_{yy} = \partial u_y / \partial y$) along with its spatial field average

(Fig. 6(b)) compared to the cross-head derived strain data. Closer examination of the spatial variations in e_{yy} during the compression load cycle reveals the emergence of localization bands (likely due to surface imperfections) which are well resolved by our 3D print pattern and the ALDIC method. Furthermore, the average compressive strain from the ALDIC compares well to the cross-head derived strain measure in the general stress-strain curve (Fig. 6(b)). Taken together, these results demonstrate the suitability of our new 3D printing technique for conducting high resolution DIC experiments.
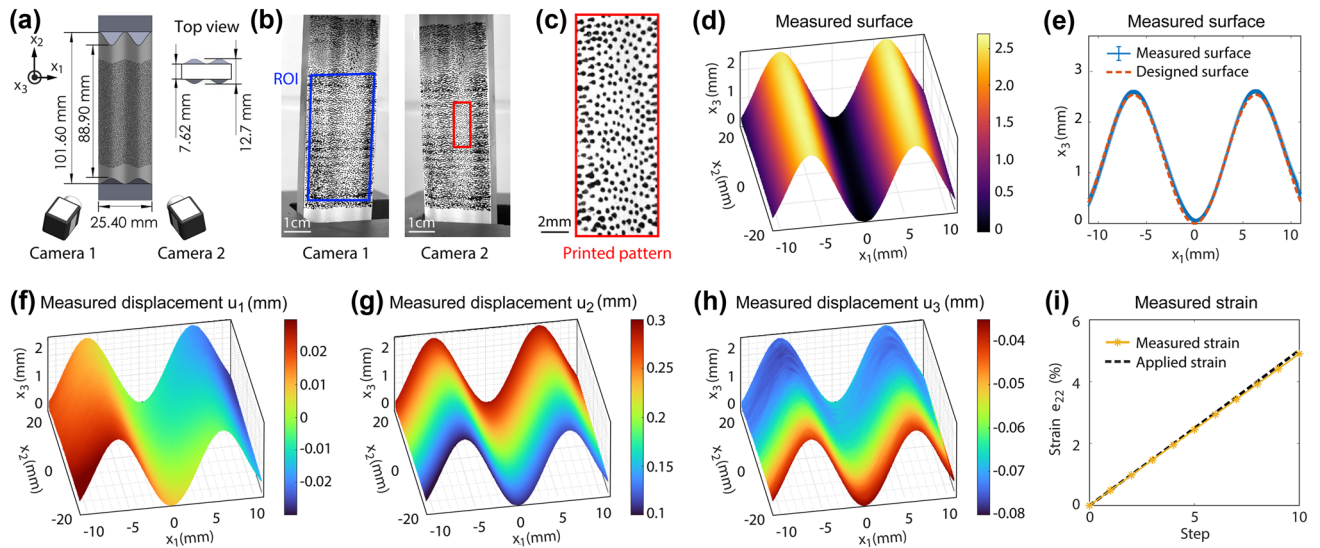

Fig. 7 3D shape, displacement and strain measurements of a 3D specimen undergoing uniaxial tension. **(a)** Schematic diagram of the 3D stereo-DIC experimental setup and the geometry of the tested non-planar, 3D sample. **(b)** Two representative camera frames are shown. A selected region of interest (ROI) is highlighted by the blue box, and the printed speckle pattern in the red box is enlarged in **(c)**. **(d)** Reconstructed specimen surface morphology via the VIC-3D algorithm. **(e)** Comparison between the mean values and standard deviations of the designed and measured surface morphologies along the x_2-axis. **(f–h)** Measured u_1, u_2, u_3 displacement fields. **(i)** Comparison between the measured tensile strain e_{22} and the applied strain calculated from the prescribed cross-head displacement

Case Study III: Uniaxial Tension of a Specimen with a 3D Topography

In addition to the previous 2D examples, we also tracked the deformation of a sample with a prescribed 3D topography undergoing uniaxial tension via 3D stereo-DIC. The non-planar specimen was 3D-printed with an elastic 50A resin (Formlabs, Somerville, MA) and its designed geometry is shown in Fig. 7(a). The top and bottom surfaces of the sample are flat to fit into the grips of the particular load frame, while the front and back faces consist of sinusoidal undulations with a double-peak shape. To improve the contrast of our speckle patterns, we first sprayed the front surface of the sample with white acrylic ink, and then printed a G-code designed, randomly distributed speckle pattern with a dot density of 4,000 dots over an area of 63.5×25.4 mm^2. Each single speckle dot has an ink extrusion volume of 3.0×10^{-7} mL, with a radius of about 130 μm.

Next, the sample was loaded in simple tension, where ten steps of 0.508 mm in cross-head displacement were applied incrementally to the specimen. During the test, two CCD cameras (FLIR Systems, Richmond, BC, Canada) and two zoom lenses (Xenoplan 1.4/17-0903, Schneider Optics Inc., Hauppauge, NY) were used to collect stereographic images of the deformation process. Two representative frames captured by the two cameras are shown in Fig. 7(b), where the printed, 3D pattern in the red box is further enlarged in Fig. 7(c). The 3D displacement field was reconstructed using the commercially available VIC-3D 2010 system (Correlated Solutions Inc., Irmo, SC) [45] by analyzing a selected region of interest (ROI), which is marked by the blue box shown in Fig. 7(b) "Camera 1". In our VIC-3D analysis, we chose a subset size of 41 px by 41 pixels with a uniform subset spacing of 8 pixels in each direction. The reconstructed specimen surface morphology is shown in Fig. 7(d−e), where a red dashed line is displaying the prescribed surface topography as printed, whereas the blue data points are showing the mean and standard deviations values of the reconstructed surface along the x_2-axis. The computed u_1, u_2, and u_3 displacement fields are summarized in Fig. 7(f−h), respectively. Next, we employed a plane fitting method with a 95% confidence interval[3] to compute the infinitesimal strain e_{22} along the principal loading direction, and compared it with the prescribed strain calculated from the cross-head displacement (Fig. 7(i)). We find that both the reconstructed, 3D surface morphology and the tracked deformation fields are in excellent agreement with the designed/applied values, demonstrating that our 3D printing technique is well-suited for generating high quality speckle patterns on non-planar 3D surfaces.

---

[3] The 95% confidence interval region is smaller than the size of the markers.

Conclusions

In this paper we present a new DIC pattern technique based on a fully customizable 3D printer. The 3D printer is controlled via easily scripted G-codes that allow for printing fully customizable DIC patterns on even complex 3D surfaces in an autonomous and automated fashion. This allows for inputting of optimal print pattern designs based on the experimental setup and the deformations to be expected. The typical printed speckle dot radius is on the order of $O(10^2)$ μm, and is well predicted by our proposed theoretical model as described in Controlling Printed Speckle Dot Size.

In order to assess the quality of the kind of print patterns that can be generated with this new 3D printing technique, we conducted DIC analyses using both synthetic and real experimental images via the typical metrics of accuracy and precision in the recovered displacement and strain fields. We find that the reconstructed DIC displacement and strain accuracy is similar to many to be considered optimal pattern designs, i.e., on the order of $O(10^{-2})$ px in measuring displacements and $O(10^{-4})$ in measuring strains. For example, the RMS error of measured displacements is within 0.015 px for deformations featuring rigid body translations, uniaxial stretch ratios less than 1.05, and pure shear angles less than 3°. Finally, we show that our 3D printer is also suitable for printing reliable DIC patterns on highly compliant and porous material surfaces undergoing large deformations with nominal compressive strains 50% ∼ 90%.

We conclude this paper with a few thoughts on advancing this work. First, in this study we have purposefully designed speckle patterns following the Poisson disc sampling procedure to avoid overlapping dot patterns. Yet, there are more complex DIC pattern design algorithms that have shown capability of producing even better reconstruction results for certain deformation scenarios [14–17, 19, 46]. These would be straightforward to implement as long as they are within the print resolution of the given printer setup, which can also be customized for inks of different surface tensions and syringe tip extrusion diameters. Second, in this paper we assessed the quality of our print pattern and the reconstruction capability of the applied material deformation using classical and advanced DIC formulations (i.e., the local subset ICGN method and the ALDIC method). However, due to the well-defined shape of our printed speckle dot patterns, advanced single particle tracking algorithms [38, 47] can also be employed to reconstruct motion fields, which opens the door to providing potentially superior reconstruction capabilities at high seeding densities compared to DIC. One of the biggest challenges when it comes to single particle tracking algorithms is the proper detection of discrete particles and accurate resolution of their centroid positions. Furthermore, by introducing two or more color extrusion heads, multi-attribute single particle tracking becomes possible, which we recently demonstrated can significantly improve the reconstruction of high frequency content under large deformations

Table 3 List of G-code commands used in controlling motor motion [35]

Command	Usage	Parameters	Example
G1	Linear move	Position (X, Y and Z), extrusion (E) and move speed (F)	G1 F200
G21	Set units to mm		G21
G28	Move to the origin		M83
G90	Use absolute coordinates		G90
G92	Set position	Position (X, Y and Z), extrusion (E)	G92 E0
M83	Set to relative mode		M83
M84	Motors off		M84
M302	Allow cold extrudes	State (P)	302
T	Select tool	Tool number	T0

or non-affine motions [38]. Third, we demonstrated that in the absence of a rotating sample stage we could print reliable speckle patterns up to surface slope angles of 30°. A straightforward modification to the current printing setup for facilitating 360° printing can be achieved by mounting the sample onto a rotating stage. Finally, we provide an open-source MATLAB function (https://github.com/FranckLab/DIC_pat_gcode) for generating various input G-code files specifically controlling the spatial arrangement and position as well as the extrusion volume for each speckle dot.

Appendix A. G-Code Commands Used in Controlling Motor Motion

A list of G-code commands used to control 3D printer motions are summarized in Table 3.

Declarations

Conflicts of Interest The authors declare that they have no conflict of interest.

References

1. Peters WH, Ranson WF (1982) Digital Imaging Techniques In Experimental Stress Analysis. Opt Eng 21:427–431
2. Pan B, Qian KM, Xie HM, Asundi A (2009) Two-dimensional digital image correlation for in-plane displacement and strain measurement: a review. Meas Sci Technol 20:62001
3. Bar-Kochba E, Toyjanova J, Andrews E, Kim K-S, Franck C (2015) A fast iterative digital volume correlation algorithm for large deformations. Exp Mech 55:261–274
4. Landauer AK, Patel M, Henann DL, Franck C (2018) A q-factor-based digital image correlation algorithm (qDIC) for resolving finite deformations with degenerate speckle patterns. Exp Mech 58:815–830
5. Yang J, Bhattacharya K (2019) Augmented Lagrangian Digital Image Correlation. Exp Mech 59:187–205
6. Dong YL, Pan B (2017) A review of speckle pattern fabrication and assessment for digital image correlation. Exp Mech 57:1161–1181
7. Yang J, Bhattacharya K (2019) Combining image compression with digital image correlation. Exp Mech 59:629–642
8. Bornert M, Hild F, Orteu JJ, Roux S (2012) Digital Image Correlation. p 157–190
9. Schreier HW, Sutton MA (2002) Systematic errors in digital image correlation due to undermatched subset shape functions. Exp Mech 42:303–310
10. Lionello G, Cristofolini L (2014) A practical approach to optimizing the preparation of speckle patterns for digital-image correlation. Meas Sci Technol 25:107001
11. Kammers AD, Daly S (2011) Small-scale patterning methods for digital image correlation under scanning electron microscopy. Meas Sci Technol 22(12):125501
12. Grant BMB, Stone HJ, Withers PJ, Preuss M (2009) High-temperature strain field measurement using digital image correlation. J Strain Anal Eng Des 44:263–271
13. Blaber J, Adair BS, Antoniou A (2015) A methodology for high resolution digital image correlation in high temperature experiments. Rev Sci Instrum 86(3):035111
14. Bossuyt S (2013) Optimized patterns for digital image correlation. In H. Jin, C. Sciammarella, C. Furlong, and S. Yoshida, editors, Imaging Methods for Novel Materials and Challenging Applications, Volume 3, pp 239–248. Springer
15. Bomarito G, Hochhalter JD, Ruggles TJ, Cannon AH (2017) Increasing accuracy and precision of digital image correlation through pattern optimization. Opt Lasers Eng 91:73–85
16. Bomarito GF, Hochhalter JD, Ruggles TJ (2018) Development of optimal multiscale patterns for digital image correlation via local grayscale variation. Exp Mech 58:1169–1180
17. Chen ZN, Shao XX, Xu XY, He XY (2018) Optimized digital speckle patterns for digital image correlation by consideration of both accuracy and efficiency. Appl Opt 57:884–893
18. Su Y, Gao ZR, Fang Z, Liu Y, Wang YR, Zhang QC, Wu SQ (2019) Theoretical analysis on performance of digital speckle pattern: uniqueness, accuracy, precision, and spatial resolution. Opt Express 27:22439–22474
19. Mathew M, Wisner B, Ridwan S, McCarthy M, Bartoli I, Kontsos A (2020) A bio-inspired frequency-based approach for tailorable and scalable speckle pattern generation. Exp Mech

20. Mazzoleni P, Zappa E, Matta F, Sutton MA (2015) Thermomechanical toner transfer for high-quality digital image correlation speckle patterns. Opt Lasers Eng 75:72–80

21. Chen ZN, Quan CG, Zhu FP, He XY (2015) A method to transfer speckle patterns for digital image correlation. Meas Sci Technol 26:95201

22. Gauvin C, Jullien D, Doumalin P, Dupre JC, Gril J (2014) Image correlation to evaluate the influence of hygrothermal loading on wood. Strain 50:428–435

23. Shafaghi N, Kapan E, Aydıner CC (2020) Cyclic strain heterogeneity and damage formation in rolled magnesium via *in situ* microscopic image correlation. Exp Mech 60:735–751

24. Özdur N, Ücel İ, Yang J, Aydıner CC (2020) Residual intensity as a morphological identifier of twinning fields in microscopic image correlation. Exp Mech 1–16

25. Turner JL, Russell SS (1990) Application of digital image analysis to strain measurement at elevated temperature. Strain 26:55–59

26. Lionello G, Sirieix C, Baleani M (2014) An effective procedure to create a speckle pattern on biological soft tissue for digital image correlation measurements. J Mech Behav Biomed Mater 39:1–8

27. Landauer AK, Li XQ, Franck C, Henann DL (2019) Experimental characterization and hyperelastic constitutive modeling of opencell elastomeric foams. J Mech Phys Solids 133:103701

28. Dong YL, Kakisawa H, Kagawa Y (2015) Development of microscale pattern for digital image correlation up to 1400 °C. Opt Lasers Eng 68:7–15

29. Koumlis S, Pagano S, Retuerta del Rey G, Kim YJ, Jewell P, Noh MJ, Lamberson L (2018) Drop on demand colloidal suspension inkjet patterning for DIC. Exp Tech 43:137–148

30. Wang HX, Xie HM, Li YJ, Zhu JG (2012) Fabrication of microscale speckle pattern and its applications for deformation measurement. Meas Sci Technol 23(3):035402

31. Scrivens WA, Luo Y, Sutton MA, Collette SA, Myrick ML, Miney P, Colavita PE, Reynolds AP, Li X (2007) Development of patterns for digital image correlation measurements at reduced length scales. Exp Mech 47:63–77

32. Li N, Guo SM, Sutton MA (2011) Recent Progress in E-Beam Lithography for SEM Patterning. MEMS and Nanotechnology. Volume 2. Springer, New York, pp 163–166

33. Walley JL, Wheeler R, Uchic MD, Mills MJ (2012) *In-Situ* Mechanical Testing for Characterizing Strain Localization During Deformation at Elevated Temperatures. Exp Mech 52:405–416

34. Hinton TJ, Jallerat Q, Palchesko RN, Park JH, Grodzicki MS, Shue HJ, Ramadan MH, Hudson AR, Feinberg AW (2015) Three-dimensional printing of complex biological structures by freeform reversible embedding of suspended hydrogels. Sci Adv 1:e1500758

35. ISO I (2009) 6983-1: Automation Systems and Integration–Numerical Control of Machines–Program Format and Definition of Address Words–Part 1: Data Format for Positioning. Line Motion and Contouring Control Systems

36. Zhou P, Goodson EK (2001) Subpixel displacement and deformation gradient measurement using digital image/speckle correlation. Opt Eng 40:1613–1620

37. Pan B, Lu ZX, Xie HM (2010) Mean intensity gradient: An effective global parameter for quality assessment of the speckle patterns used in digital image correlation. Opt Lasers Eng 48:469–477

38. Patel M, Leggett SE, Landauer AK, Wong IY, Franck C (2018) Rapid, topology-based particle tracking for high-resolution measurements of large complex 3D motion fields. Sci Rep 8:5581

39. Brakke AK (1992) The surface evolver. Exp Math 1:141–165

40. Levoy M, Pulli K, Curless B, Rusinkiewicz S, Koller D, Pereira L, Ginzton M, Anderson S, Davis J, Ginsberg J et al (2000) The digital michelangelo project: 3d scanning of large statues. In Proceedings of the 27th annual conference on Computer graphics and interactive techniques, pp 131–144

41. Yang J, Wang A, Zheng QS (2017) Ultra-long lifetime water bubbles stabilized by negative pressure generated between microparticles. Soft Matter 13:8202–8208

42. Bornert M, Doumalin P, Dupré JC, Poilâne C, Robert L, Toussaint E, Wattrisse B (2017) Shortcut in DIC error assessment induced by image interpolation used for subpixel shifting. Opt Lasers Eng 91:124–133

43. Yang J, Bhattacharya K (2021) Fast adaptive mesh augmented Lagragian digital image correlation. Exp Mech 1-17

44. Reu PL, Toussaint E, Jones E, Bruck HA, Iadicola M, Balcaen R, Turner DZ, Siebert T, Lava P, Simonsen M (2018) DIC challenge: Developing images and guidelines for evaluating accuracy and resolution of 2D analyses. Exp Mech 58:1067–1099

45. Solutions, Correlated. "Vic-3D v7 Reference Manual." Correlated Solutions (2014).

46. Grédiac M, Blaysat B, Sur F (2020) On the optimal pattern for displacement field measurement: Random speckle and dic, or checkerboard and LSA. Exp Mech 60:509–534

47. Qi Y, Zou ZN, Xiao JL, Long R (2019) Mapping the nonlinear crack tip deformation field in soft elastomer with a particle tracking method. J Mech Phys Solids 125:326–346